



# An efficient approach to develop and screen out high-entropy alloy composition with high performance for biomedical application

Xuan Xiao, Manzhen Lin, Chenhao Xu, Jiawei Zhang, Wei-Bing Liao\*

*Key Laboratory of Optoelectronic Devices and Systems of Ministry of Education and Guangdong Province, College of Physics and Optoelectronic Engineering, Shenzhen University, Shenzhen 518060, China*

## ARTICLE INFO

**Keywords:**  
High-entropy alloys  
Composition  
Microstructures  
Mechanical properties  
Corrosion resistance

## ABSTRACT

High-entropy alloys (HEAs) have great prospects for applications as biomedical materials due to their excellent properties of high strength and corrosion resistance. In this study, a co-deposition technology with two targets was used to prepare 16 independent Ti-Zr-Nb-Ta HEA samples with composition gradient distribution. Afterwards, these samples' chemical compositions, structures, and properties were systematically studied, and it was found that there was a non-linear relationship between the compositions, structures, and properties. The chemical composition of  $Ti_{12.50}Zr_{11.56}Nb_{12.71}Ta_{46.62}O_{16.61}$  HEA sample with superior comprehensive properties was efficiently screened out, and its nanohardness, open circuit potential (OCP) value, and corrosion current density were identified to be 12.91 GPa,  $-0.37$  V<sub>SCE</sub>, and  $3.91 \times 10^{-9}$  A·cm<sup>-2</sup>, respectively. This parallel co-deposition method offered a new efficient approach to develop advanced biomedical HEAs.

## 1. Introduction

Biomedical metals such as Ti6Al4V alloy, CoCrMo alloy, and 316 L stainless steel [1] have a great demand for surgical implant applications. In current clinical trials, it has been found that the TiO<sub>2</sub> oxide film that formed on the Ti6Al4V surface during practical orthopedic implant application is easily damaged and loses its protection, which would lead to an increase in the content of Al and V ions around the implant, resulting in adverse reactions such as neurological abnormalities, osteomalacia, and Alzheimer's disease, as well as adverse effects on osseointegration [2–6]. Moreover, Ti6Al4V has low hardness, insufficient wear resistance, and high friction coefficient. The debris generated by wear could also cause inflammation and release of bone-dissolving agents, leading to bone dissolution around the prosthesis and causing metal allergy, cell toxicity, DNA damage, etc. [6–9]. Thus, considering above deficiencies of Ti6Al4V alloy, it has been an emergent case to develop new kinds of advanced metals with high corrosion resistance, excellent mechanical properties, and good biocompatibility. Since high-entropy alloys (HEAs) concept was first reported in 2004 [10], this new alloy concept has attracted extensive attention. Due to their very high mixing entropy, HEAs often tend to form simple solid solution phase structures such as face-centered cubic (FCC) or body-centered cubic (BCC) [11–15]. The unique crystal structure of HEAs brings many

properties superior to traditional alloys such as high hardness, strong corrosion resistance and high strength [16–19]. Therefore, HEAs have a great potential for biomedical application in the future.

However, the composition design and optimization of HEAs are complex. Currently, the “trial and error method” is mainly used in research, and only one sample with a single composition can be prepared in one experiment. Otherwise, multiple experiments need to be repeated to prepare samples with multiple compositions, which has the disadvantages of long-time consumption, long research cycle, high cost, and low efficiency [20]. Therefore, there is an urgent need for a high-throughput processing technology to improve efficiency. In the 1970s, J.J. Hanak [21] first proposed an experimental scheme with “high throughput” characteristics. High-throughput preparation, also known as combinatorial preparation, refers to a method to prepare a large number of samples in a short period of time, forming a material library containing a certain range of compositions. To date, thin film deposition is the most commonly used method for high-throughput preparation, mainly including co-deposition [21], separated template coating [22], continuous phase diagram template coating [23], and machine learning [24]. Among them, co-deposition technology is the most suitable method for high-throughput preparation of HEAs. When the distance between the target and the substrate is different, the probability of target atoms depositing near the target is higher, resulting in the formation of

\* Corresponding author.

E-mail address: [liaowb@szu.edu.cn](mailto:liaowb@szu.edu.cn) (W.-B. Liao).



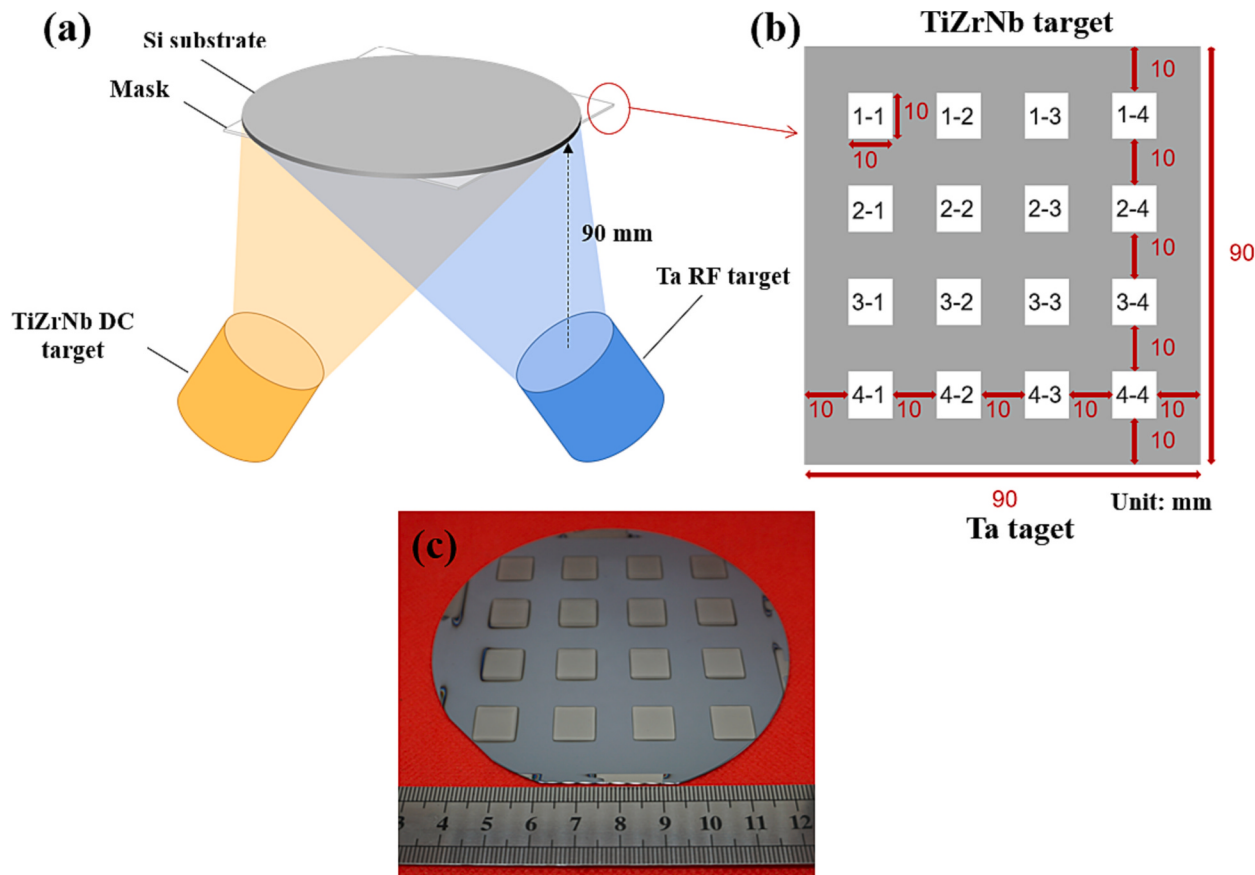


**Fig. 1.** (a) schematic diagram of the preparation of Ti-Zr-Nb-Ta HEA samples by dual-target co-deposition; (b) schematic diagram of the mask used in the work; (c) 16 independent Ti-Zr-Nb-Ta HEA samples.

**Table 1**

Average atomic percentages of each element, sample thickness, deposition rate and mixture entropy  $\Delta S_{\text{mix}}$  of 16 independent Ti-Zr-Nb-Ta HEA samples, R represents the molar gas constant.

Sample	Ti (at. %)	Zr (at. %)	Nb (at. %)	Ta (at. %)	O (at. %)	Thickness (nm)	Deposition rate (nm·min <sup>-1</sup> )	$\Delta S_{\text{mix}}$ (kJ·mol <sup>-1</sup> )
1-1	20.01	18.69	18.73	29.38	13.19	990.0	16.50	1.58 R
1-2	20.96	16.14	15.57	29.22	18.11	1064.0	17.73	1.58 R
1-3	21.82	19.18	18.91	27.39	12.70	1012.0	16.87	1.58 R
1-4	19.30	17.04	17.39	30.28	15.99	930.4	15.51	1.58 R
2-1	12.25	10.31	10.89	50.02	16.53	774.1	12.90	1.38 R
2-2	12.96	12.62	12.86	46.33	15.23	908.1	15.14	1.43 R
2-3	12.99	10.60	10.78	49.07	16.56	826.2	13.77	1.39 R
2-4	12.50	11.56	12.71	46.62	16.61	811.3	13.52	1.43 R
3-1	6.52	5.97	6.62	62.78	18.11	856.0	14.27	1.13 R
3-2	7.21	6.66	7.41	63.93	14.79	893.2	14.89	1.13 R
3-3	6.00	5.92	6.68	66.24	15.16	684.8	11.41	1.08 R
3-4	6.51	5.94	6.81	65.18	15.56	774.1	12.90	1.10 R
4-1	3.37	2.29	3.48	78.59	12.27	967.6	16.13	0.76 R
4-2	1.74	1.12	1.37	85.80	9.97	558.2	9.30	0.54 R
4-3	2.65	1.34	2.12	86.73	7.16	818.8	13.65	0.55 R
4-4	3.68	1.73	1.99	81.74	10.86	960.2	16.00	0.68 R

films with different compositions on the substrate. X.G. Feng et al. [25] prepared ZrNbTaTiW refractory HEA thin films by co-sputtering of two alloy targets and a pure Zr target. The power and target spacing directly affect the deposition rate and film composition, and three morphologies, amorphous, columnar, and equiaxed, can be observed. The maximum hardness and elastic modulus of the ZrNbTaTiW thin film reached 11.5 GPa and 190.4 GPa, respectively. Y. Zhang et al. [26] achieved the parallel preparation of Ti-Nb-Zr HEAs through three-target co-deposition, and the substrate was divided into 144 small squares with an area of 1 cm<sup>2</sup>. Each small square was considered as an independent “sample unit”, and the average variation range of each element content in the

144 sample units was 3.34 at. % to 89.25 at. %. The above experimental studies have shown that high-throughput experiments based on co-deposition can effectively prepare a series of independent HEA samples with different compositions, which can be further screened quickly and accurately through subsequent characterization. This co-deposition preparation method makes the magnetic sputtering process more flexible, overcomes the difficulty of preparing some multi-component alloy targets, and can adjust the chemical composition by adjusting the power, position, angle, and combination of targets.

The metal elements with good biocompatibility are quite limited, such as Ti, Zr, Nb, Ta, Mo, Hf, Sn, etc. [27]. To date, researchers have

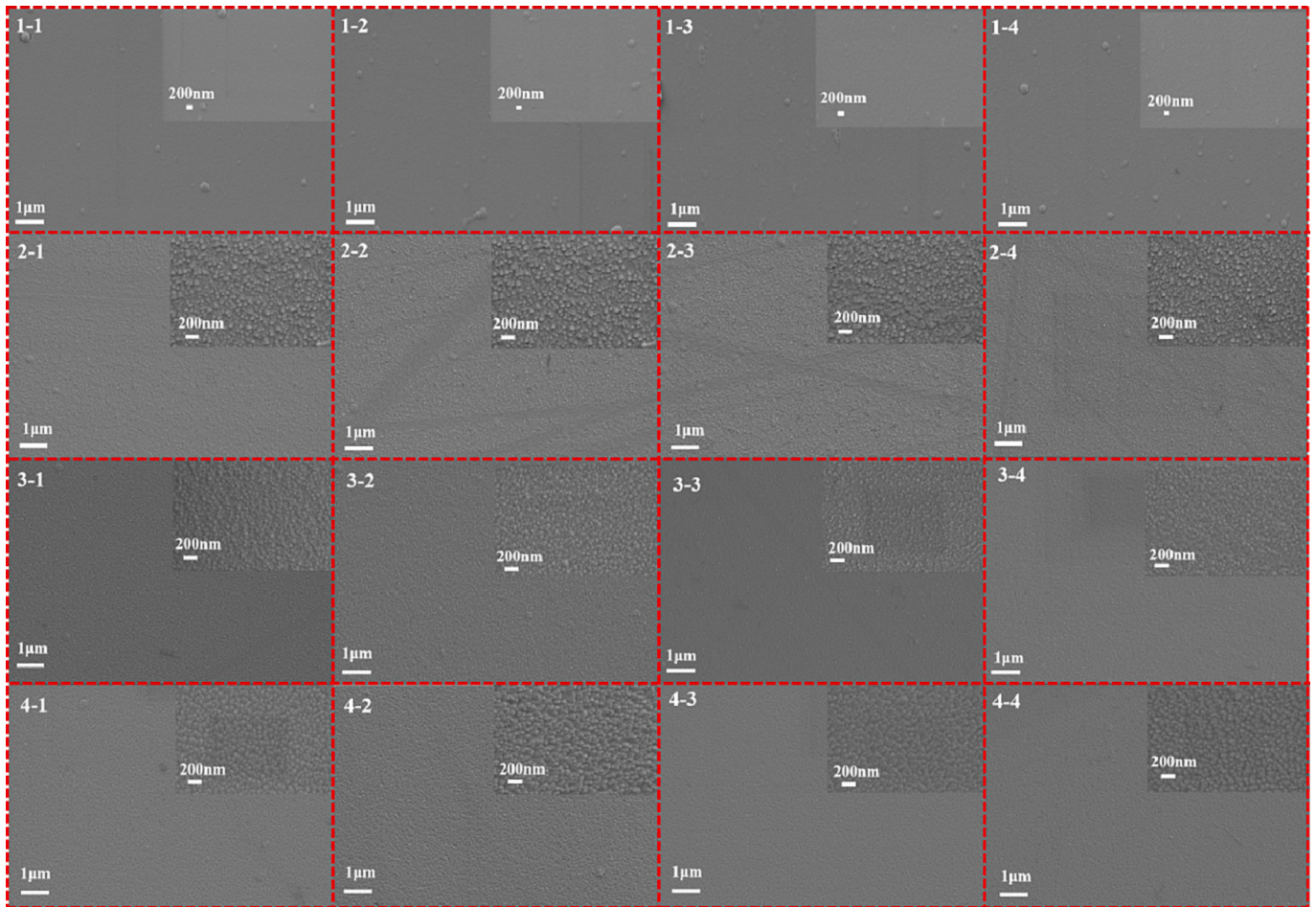


**Fig. 2.** SEM surface morphologies of 16 independent Ti-Zr-Nb-Ta HEA samples.

made some significant progress in the development of biomedical HEAs. Q.T. Song et al. [28] studied the electrochemical behavior of (TiZrNb-Ta)<sub>90</sub>Mo<sub>10</sub> alloy at different pH values and found that its corrosion resistance in simulated physiological environment was significantly better than conventional implant metals, such as 316 L stainless steel and CoCrMo. N. Hua et al. [29] studied the mechanical properties and corrosion resistance of Ti<sub>x</sub>ZrNbTaMo alloy in simulated physiological environment, and the results showed that all Ti<sub>x</sub>ZrNbTaMo exhibited a low corrosion rate comparable to Ti6Al4V, among which Ti<sub>0.5</sub>ZrNb-TaMo showed the best mechanical properties and the highest corrosion resistance. Therefore, compared with traditional medical alloys, new biomedical HEAs have advantages in hardness, corrosion resistance and biocompatibility, and are expected to become a new generation of biomedical alloy materials. However, the current research on new biomedical HEAs is still in infancy, and the quantitative relationship between their composition, phase structure, and mechanical properties needs further systematic research. It's reported that Ti, Nb and Ta had excellent osteointegration and blood compatibility with almost no cytotoxicity, and Zr would almost not respond to surrounding cells due to the stable oxides form on its surface [30,31]. In this work, we selected Ti, Zr, Nb and Ta elements with good biocompatibility, and used a new dual-target co-deposition technique to develop 16 independent Ti-Zr-Nb-Ta biomedical HEA samples with compositional gradient distribution, enabling efficient screening of medical material compositions with excellent performance.

## 2. Experimental procedures

### 2.1. Materials preparation

Ti-Zr-Nb-Ta HEA samples were deposited by magnetron sputtering (JGP-450, SKY Technology Development CO., LTD. Chinses Academy of Sciences). The dual-target co-deposition technique for preparing the Ti-Zr-Nb-Ta HEA samples was illustrated in Fig. 1(a). The TiZrNb target (prepared by hot pressing sintering, size Φ 60 mm × 5 mm, purity ≥99.9 %) was powered by a direct current (DC) power supply with a power of 100 W, and the Ta target (prepared by hot pressing sintering, size Φ 60 mm × 5 mm, purity ≥99.95 %) was powered by a radio frequency (RF) power supply with a power of 160 W. A single-sided polished single crystal silicon (111) with a diameter size of 100 ± 0.4 mm and a thickness of 500 ± 25 μm was selected as the substrate. To remove pollutants from the substrate surface, the substrate was placed in deionized water, acetone, and anhydrous ethanol for ultrasonic cleaning for 10 min, respectively. Then high-purity Ar was used to dry the substrate. The substrate was set in the middle position of the two targets. The relative position of the two targets was maintained at 180°, and the vertical distance between the targets and the substrate was 90 mm. To obtain independent samples with different chemical compositions, a stainless-steel mask with 4 × 4 holes was placed on the substrate. Each hole had a square shape with a size of 10 mm × 10 mm, and the spacing between adjacent holes was also 10 mm, as shown in Fig. 1(b). Before deposition, the chamber was evacuated to 5 × 10<sup>-4</sup> Pa, then Ar with a flow rate of 40 standard cubic centimeters per minute (sccm) was introduced into the chamber. The working pressure was controlled at 0.5 Pa. Prior to formal deposition, the baffle was closed for pre-

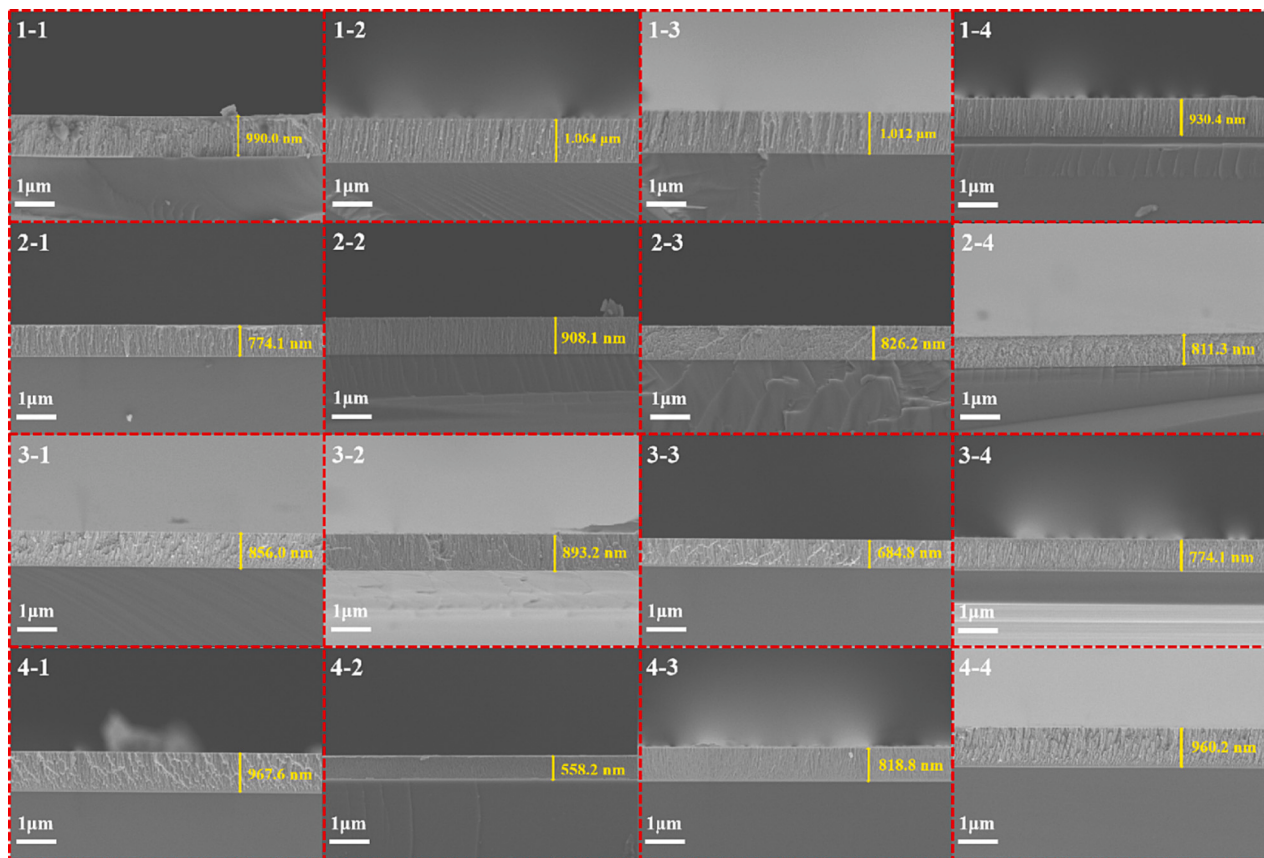


**Fig. 3.** SEM cross-sectional morphology of 16 independent Ti-Zr-Nb-Ta HEA samples.

sputtering for 5 min. Afterwards, the Ti-Zr-Nb-Ta HEA samples were prepared by dual-target co-deposition technique for 1 h. Finally, 16 independent Ti-Zr-Nb-Ta HEA samples with composition gradient distributions were prepared, as shown in Fig. 1(c). To describe the samples clearly, we assign a unique identity document (ID) number to each sample grid, and name each sample in the form of X-Y (row X, column Y) (X ranges from 1 to 4, and Y ranges from 1 to 4), as shown in Fig. 1(b).

## 2.2. Composition and microstructure analysis

The thickness, cross-sectional microstructure, and surface morphology of the Ti-Zr-Nb-Ta HEA samples were determined using a thermal field scanning electron microscope (SEM, Supra 55 Sapphire), and the compositions were measured using a automated energy dispersive X-ray (EDX) at 15 KeV. The phase structures were detected by X-ray diffractometer (XRD, Xpertpro), and Cu K $\alpha$  ( $\lambda = 0.154060$  nm) was used as the X-ray source, with a tube voltage of 40 kV and a tube current of 40 mA. A continuous scanning mode was used, with a scanning speed of 2°/min, and the grazing incidence angle for grazing incidence X-ray diffraction was 4°.

## 2.3. Mechanical properties

The nanohardness (H) and elastic modulus (E) of the Ti-Zr-Nb-Ta HEA samples were measured at room temperature using a nanoindentation instrument (HysitronTI - 950) with a Berkovich diamond indenter. The loading and unloading times were both 5 s, and the holding time was 2 s. The maximum load was 900  $\mu$ N. To avoid the influence of the substrate on the experimental results, the effective indentation depth was controlled to be <10 % of the film sample thickness, and 16 points were measured for each sample to obtain the average value.

## 2.4. Electrochemical corrosion testing

The electrochemical corrosion performance of the Ti-Zr-Nb-Ta HEA samples were measured using an electrochemical workstation (CHI760). A traditional three-electrode system was used, in which the saturated calomel electrode (SCE) was used as the reference electrode, the platinum sheet was used as the counter electrode, and the test sample with an exposed area of 1  $\text{cm}^2$  was used as the working electrode. Phosphate buffer solution (PBS) was selected to simulate body fluid as the electrochemical corrosion solution for electrochemical experiments, and the solution temperature was controlled at  $37 \pm 0.5$  °C. The proportion of the PBS contained 8 g/L NaCl, 0.2 g/L KCl, 1.15 g/L Na<sub>2</sub>HPO<sub>4</sub> and 0.2 g/L KH<sub>2</sub>PO<sub>4</sub>. For open circuit potential (OCP) tests, the Ti-Zr-Nb-Ta HEA samples were immersed in PBS at 37 °C for 60 min to detect the evolution of OCP, and for potentiodynamic polarization tests, the testing range of the samples was 0.3 V below the E<sub>OCP</sub> to 1.2 V, and the scanning rate was 1 mV/s.

## 3. Results and discussion

### 3.1. Sample compositions and morphologies

**Table 1** lists the average atomic percentages of 16 independent Ti-Zr-Nb-Ta HEA samples. It can be seen that the atomic percentages of Zr and Nb are comparable, while the atomic percent of Ti is slightly higher than that of Zr and Nb. This is because the atomic weights of Zr (91.224) and Nb (92.906) are comparable, while the atomic weight of Ti (47.867) is lower than that of Zr and Nb. Sputtering is a momentum transfer controlled process, and atoms with a lower atomic weight in the alloy target are more likely to sputter from the target surface. From **Table 1**, it can be seen that the atomic percentage of Ta in the same row fluctuates slightly, while the atomic content of Ta in different rows varies greatly.

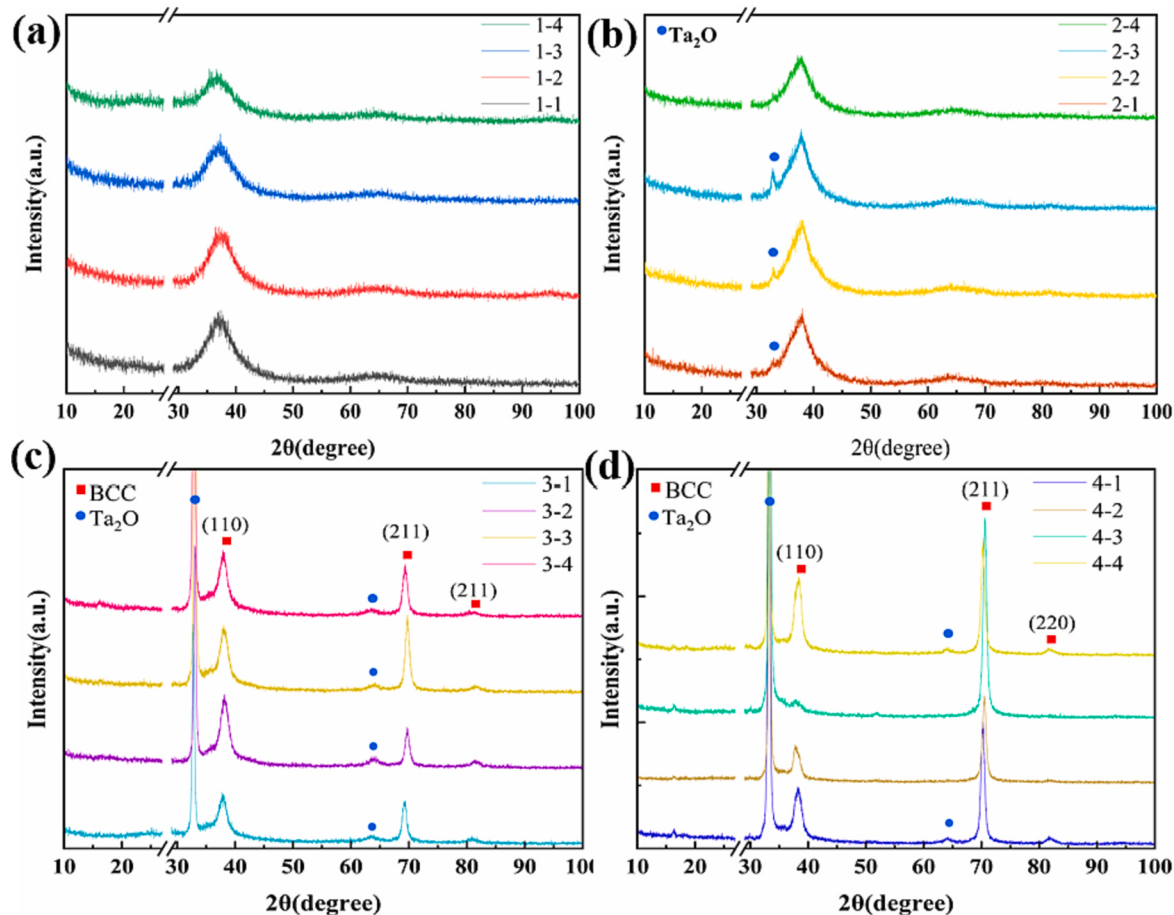


Fig. 4. XRD pattern of the first row (a), second row (b), third row (c), and fourth row(e) of 16 independent Ti-Zr-Nb-Ta HEA samples.

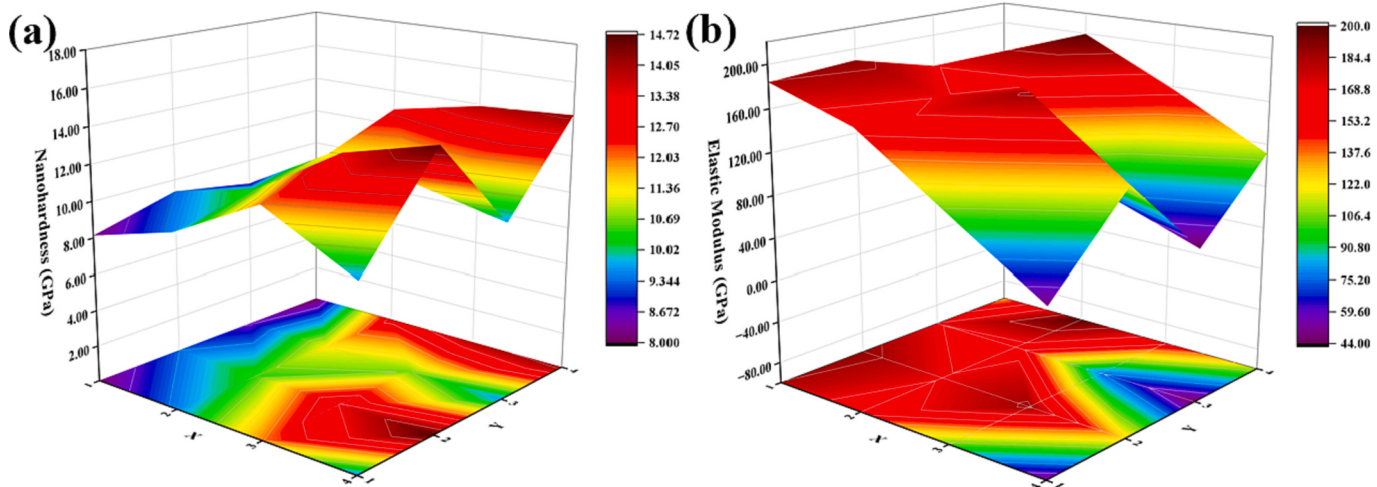


Fig. 5. 3D distribution diagram of nanohardness (a) and elastic modulus (b) of 16 independent Ti-Zr-Nb-Ta HEA samples with different compositions.

The closer to the samples in the fourth row, the higher the atomic percentage of Ta. This was mainly due to the distance between the Ta target and the sample. As shown in Fig. 1, the HEA samples in the fourth row were closest to the Ta target, and the closer to the Ta target, the higher the content of Ta in the samples. This phenomenon can also be seen in Ti, Zr, and Nb elements. The TiZrNb target is closest to the sample in the first row, so from the samples in the first row to the fourth row, the content of Ti, Zr, Nb, and other elements gradually decreases. Moreover, it was found that each sample contained approximately 14 at. % Oxygen

(minor content, approximately 2 wt%), which is mainly because the TiZrNb target and Ta target formed by hot pressing sintering tends to retain oxygen as well as the oxygen affinity of Ta metal.

Fig. 2 shows the SEM surface morphologies of 16 independent Ti-Zr-Nb-Ta HEA samples with different compositions. The samples of the same row have similar micro-surface morphology due to their similar chemical composition, while the samples in the different rows have very different surface morphology due to large differences in Ta content. The surface of the samples in the first row (1-1, 1-2, 1-3, 1-4) is very smooth

**Table 2**

Mechanical properties and corrosion resistance of 16 independent Ti-Zr-Nb-Ta HEA samples.

Sample	Nanohardness (GPa)	Elastic Modulus (GPa)	$E_{OCP}$ (V <sub>SCE</sub> )	$E_{corr}$ (V <sub>SCE</sub> )	$I_{corr}$ (A·cm <sup>-2</sup> )
1-1	$8.14 \pm 0.65$	$184.05 \pm 9.96$	-0.42	-0.50	$4.76 \times 10^{-9}$
1-2	$9.34 \pm 0.31$	$189.35 \pm 6.85$	-0.44	-0.56	$7.24 \times 10^{-9}$
1-3	$8.61 \pm 0.37$	$169.31 \pm 3.37$	-0.42	-0.53	$5.53 \times 10^{-9}$
1-4	$8.00 \pm 0.40$	$132.81 \pm 4.82$	-0.39	-0.51	$5.92 \times 10^{-9}$
2-1	$9.48 \pm 1.09$	$159.09 \pm 13.33$	-0.30	-0.43	$4.22 \times 10^{-9}$
2-2	$10.45 \pm 0.75$	$169.72 \pm 7.88$	-0.34	-0.44	$5.03 \times 10^{-9}$
2-3	$11.31 \pm 0.61$	$163.19 \pm 4.02$	-0.31	-0.43	$4.23 \times 10^{-9}$
2-4	$12.91 \pm 0.65$	$199.57 \pm 6.99$	-0.37	-0.50	$3.91 \times 10^{-9}$
3-1	$12.00 \pm 1.03$	$103.23 \pm 4.69$	-0.36	-0.43	$8.20 \times 10^{-9}$
3-2	$13.41 \pm 0.98$	$186.41 \pm 12.38$	-0.40	-0.53	$5.77 \times 10^{-9}$
3-3	$10.71 \pm 0.98$	$76.18 \pm 3.93$	-0.39	-0.52	$4.83 \times 10^{-9}$
3-4	$13.91 \pm 0.74$	$157.66 \pm 4.21$	-0.40	-0.53	$5.23 \times 10^{-9}$
4-1	$9.55 \pm 0.46$	$48.18 \pm 1.26$	-0.39	-0.49	$6.90 \times 10^{-9}$
4-2	$14.72 \pm 0.76$	$123.78 \pm 4.04$	-0.42	-0.50	$7.67 \times 10^{-9}$
4-3	$9.61 \pm 0.91$	$44.34 \pm 2.07$	-0.40	-0.53	$4.41 \times 10^{-9}$
4-4	$14.22 \pm 1.15$	$111.16 \pm 5.02$	-0.37	-0.43	$8.20 \times 10^{-9}$

and flat, with some nanoparticles intermingled. As the Ta content increases, the surface of the samples in the second row (2-1, 2-2, 2-3, 2-4) begins to cover some nanoparticles, and the surface of the sample becomes rough. As the Ta content further increases, the surface of the samples in the third row (3-1, 3-2, 3-3, 3-4) is completely covered by dome-shaped nanoparticles, and the surface of the samples in the fourth row (4-1, 4-2, 4-3, 4-4) has larger particles, and the surface becomes needle-like nanoparticles.

During the same deposition time, as shown in Fig. 3 and Table 1, 16 samples have different thicknesses, indicating that these samples have different deposition rates. The deposition rate is related to the deposition efficiency, and the specific values are listed in Table 1. It can be seen that the deposition rates of the samples range from  $9.30 \text{ nm} \cdot \text{min}^{-1}$  to  $17.73 \text{ nm} \cdot \text{min}^{-1}$ . The different deposition rates of the samples could be ascribed to the different distances between the substrates and the target. All samples can clearly observe a columnar structure along the growth direction, which is a typical characteristic of the deposition process of magnetron sputtering. Among them, at higher deposition rates, the mobility of adsorbed atoms on the growing film can be enhanced to allow the diffusion of underlying crystals or grains. Therefore, as the deposition rate increases, the atomic mobility increases and the columnar structure becomes more complete.

### 3.2. Phase structures

Fig. 4 shows the XRD patterns of 16 independent Ti-Zr-Nb-Ta HEA samples. In order to avoid the additional peak interference of the single crystal silicon substrate (111) at  $2\theta = 28^\circ$ , and to clearly display the XRD peaks, all XRD patterns were set with a breakpoint at  $2\theta = 27^\circ \sim 29^\circ$ . Fig. 4(a) shows the XRD pattern of the samples in the first row, where a broadened peak can be seen in the range of  $2\theta = 30^\circ \sim 45^\circ$ , indicating that the samples in the first row were severely amorphous, and the

samples were in an amorphous structure. This is mainly due to the high cooling rate during the dual-target co-deposition process. Fig. 4(b) shows the XRD pattern of the samples in the second row, where a broad peak can also be seen in the range of  $2\theta = 30^\circ \sim 45^\circ$ . Compared to the samples in the first row, the broad peak is sharper, indicating that with the increase of Ta content, the amorphous structure begins to have a crystallization trend. It is worth noting that there is a small peak near  $33^\circ$  in samples 2-1, 2-2, 2-3, which is caused by  $\text{Ta}_2\text{O}$ . Since Ta is a very oxygen-loving element, even under oxygen-deficient conditions, it can form a stable passivation film [32]. Therefore, the excess Ta atoms begin to combine with oxygen atoms to form  $\text{Ta}_2\text{O}$  compounds.

The mixing entropy  $\Delta S_{mix}$  of HEAs can be calculated by following equation [33]:

$$\Delta S_{mix} = -R \sum_{i=1}^n c_i \ln c_i \quad (1)$$

where R is the molar gas constant ( $R = 8.314 \text{ J}/(\text{mol} \cdot \text{K})$ ), n is the number of alloy components, and  $c_i$  is the compositional content of the ith component. The calculated values of the mixing entropy  $\Delta S_{mix}$  for each sample are shown in Table 1. It can be seen that the  $\Delta S_{mix}$  of 16 independent Ti-Zr-Nb-Ta HEA samples is between  $0.54 \text{ R}$  and  $1.58 \text{ R}$ , indicating that the samples have the high entropy, medium entropy, and low entropy ranges, and as the content of Ta increases, the  $\Delta S_{mix}$  of the samples decreases.

With the further increase in Ta content, the samples in the third row are fully crystallized, as shown in Fig. 4(c). There are  $\text{Ta}_2\text{O}$  peaks near  $33^\circ$  and  $64^\circ$  in XRD, and the atomic percentage of Ta in the samples in the third row exceeds 60 at. %, resulting in a significant decrease in the  $\Delta S_{mix}$ . This leads to a sharp increase in the intensity of the diffraction peak near  $33^\circ$  in  $\text{Ta}_2\text{O}$ , and diffraction peaks appear near  $38^\circ$ ,  $70^\circ$ , and  $81^\circ$ , corresponding to the (110), (211), and (220) diffraction peaks of the BBC phase. It is worth noting that the BCC phase of 3-2 and 3-4 has a preferential orientation of (110), while the BCC phase of 3-1 and 3-3 has a preferential orientation of (211). The samples in the fourth row are almost dominated by Ta elements, and the XRD of these samples is similar to that of the samples in the third row, with the presence of  $\text{Ta}_2\text{O}$  intermetallic compounds and the BCC phase, as shown in Fig. 4(d). However, compared to the samples in the third row, the (211) diffraction peak of the BBC phase has a significant enhancement, and the preferential orientation of the samples in the fourth row is (211), among which the (211) preferential orientation of the BBC phase in 4-1 and 4-3 is the most obvious. Overall, using dual-target co-deposition, 16 independent HEA samples were identified to have three different kinds of phases: amorphous, amorphous and  $\text{Ta}_2\text{O}$ , as well as BCC solid solution and  $\text{Ta}_2\text{O}$ .

### 3.3. Composition screening

To meet the needs for biomedical applications, the sample's composition with excellent mechanical properties and corrosion properties was further to screen out from the 16 independent HEA samples.

#### 3.3.1. Screening composition by mechanical properties

The biomedical alloys generally need to have good wear resistance, and hardness is an important parameter to evaluate this property. Fig. 5 shows the distribution of nanohardness and elastic modulus of 16 independent Ti-Zr-Nb-Ta HEA samples with different compositions. The specific values are shown in Table 2. It can be seen that the nanohardness of the samples in the second row increases compared to the samples in the first row, which may be due to the formation of amorphous and  $\text{Ta}_2\text{O}$  compound structures. It is worth noting that there are large fluctuations in the nanohardness and elastic modulus between the samples in the third and fourth rows, while the Ta atomic percentage is closed to each other. The hardness of 3-1 and 3-3 is lower than that of 3-2 and 3-4, and the elastic modulus is significantly lower than that of 3-2 and 3-4. It

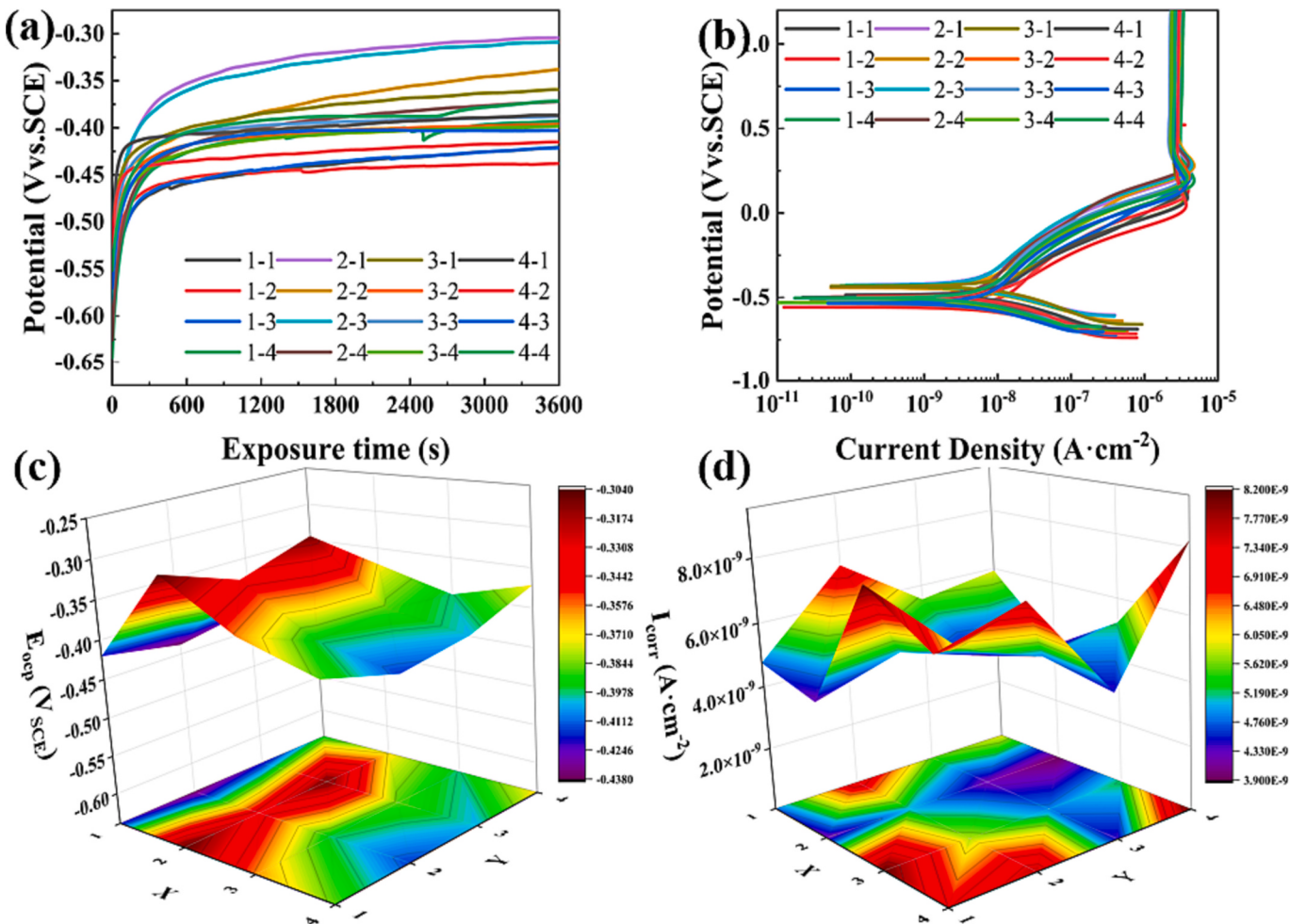


**Fig. 6.** (a) OCP curves, (b) potentiodynamic polarization curves, (c) 3D distribution diagram of  $E_{OCP}$ , and (d) corrosion current density of Ti-Zr-Nb-Ta HEA samples with 16 different compositions.

can be also found that elastic modulus of samples 4-1 and 4-3 are  $\sim 48.18$  GPa and  $\sim 44.34$  GPa, respectively, which are very low and have great potential for biomedical applications. This phenomenon of large fluctuations in performance also exists in samples in the fourth row, where the nanohardness and elastic modulus of samples 4-1 and 4-3 are lower than those of samples 4-2 and 4-4. Therefore, five highest nanohardness samples were initially screened out: sample 4-2 ( $14.72 \pm 0.76$  GPa), sample 4-4 ( $14.22 \pm 1.15$  GPa), sample 3-4 ( $13.91 \pm 0.74$  GPa), sample 3-2 ( $13.41 \pm 0.98$  GPa), and sample 2-4 ( $12.91 \pm 0.65$  GPa).

### 3.3.2. Screening composition by corrosion resistance

To further screen out the best sample for biomedical application, corrosion properties were systematically studied. Since the alloys would be exposed to human body fluids for biomedical application, the PBS was used at  $37^\circ\text{C}$  to simulate human body fluids, then electrochemical tests were conducted on the alloy samples. The typical OCP values and corrosion current density of the samples were selected to represent their corrosion resistance. Fig. 6(a) shows the OCP curves of 16 independent Ti-Zr-Nb-Ta HEA samples immersed in PBS at  $37^\circ\text{C}$  for 1 h. It can be seen that the potential increases rapidly in the beginning for a short period of time, and then reaches a stable value. The OCP values at this time called  $E_{OCP}$ , and they were listed in Table 2. In order to more intuitively observe the distribution of  $E_{OCP}$ , 3D distribution diagram of  $E_{OCP}$  is shown in Fig. 6(c). It can be seen that the  $E_{OCP}$  of the samples in the first row is between  $-0.39$  and  $-0.44$  V<sub>SCE</sub>. As the Ta content increases, the  $E_{OCP}$  of the samples in the second row moves in a more

positive direction, between  $-0.30$  and  $-0.37$  V<sub>SCE</sub>, reaching a maximum, indicating that the samples in the second row have the smallest corrosion tendency overall. The maximum  $E_{OCP}$  at this time is attributed to the combined effect of the overall amorphous structure and the appropriate amount of Ta. The amorphous structure is more stable in corrosive environment due to the absence of grain boundaries, while the higher Ta content in the samples in the second row can contribute to the formation of stable  $\text{Ta}_2\text{O}_5$  passivation film on the sample's surface in corrosive environments [32]. The  $E_{OCP}$  of the samples in the third row is between  $-0.36$  and  $-0.40$  V<sub>SCE</sub>, which is comparable to the  $E_{OCP}$  of the samples in the fourth row ( $-0.37$  to  $-0.42$  V<sub>SCE</sub>). The larger the  $E_{OCP}$ , the higher its thermodynamic stability, and the lower the corrosion sensitivity of the sample. Thus, the highest  $E_{OCP}$  of the 16 independent samples were screened out to be samples 2-1 ( $-0.30$  V<sub>SCE</sub>), sample 2-3 ( $-0.31$  V<sub>SCE</sub>), sample 2-2 ( $-0.34$  V<sub>SCE</sub>), sample 3-1 ( $-0.36$  V<sub>SCE</sub>), sample 2-4 ( $-0.37$  V<sub>SCE</sub>) and sample 4-4 ( $-0.37$  V<sub>SCE</sub>).

Generally, corrosion current density represents the corrosion rate, and the smaller the corrosion current density, the lower the corrosion rate. Fig. 6(b) shows the potentiodynamic polarization curves of 16 independent Ti-Zr-Nb-Ta HEA samples with different compositions. The lower part of the curve represents the cathodic polarization curve, and the upper part represents the anodic polarization curve. From the potentiodynamic polarization curves, the corrosion potential ( $E_{corr}$ ) and corrosion current density ( $i_{corr}$ ) of 16 independent Ti-Zr-Nb-Ta HEA samples can be obtained. The specific values are shown in Table 2. To observe the distribution of corrosion current density clearly, the 3D distribution diagram of corrosion current density is shown in Fig. 6(d).

There is a nonlinear relationship between the corrosion current density and the composition of the sample. The samples with relative lower values of the corrosion current density were screened out to be sample 2-4 ( $3.91 \times 10^{-9} \text{ A}\cdot\text{cm}^{-2}$ ), sample 2-1 ( $4.22 \times 10^{-9} \text{ A}\cdot\text{cm}^{-2}$ ), sample 2-3 ( $4.23 \times 10^{-9} \text{ A}\cdot\text{cm}^{-2}$ ), sample 4-3 ( $4.41 \times 10^{-9} \text{ A}\cdot\text{cm}^{-2}$ ) and sample 1-1 ( $4.76 \times 10^{-9} \text{ A}\cdot\text{cm}^{-2}$ ).

Considering the nanohardness, OCP, and corrosion current density, sample 2-4 with a chemical composition of  $\text{Ti}_{12.50}\text{Zr}_{11.56}\text{Nb}_{12.71}\text{Ta}_{46.62}\text{O}_{16.61}$  was screened out to possess the best comprehensive performance, which exhibited a nanohardness of  $12.91 \pm 0.65 \text{ GPa}$ , an  $E_{\text{OCP}}$  of  $-0.37 \text{ V}_{\text{SCE}}$ , and a minimum corrosion current density of  $3.91 \times 10^{-9} \text{ A}\cdot\text{cm}^{-2}$ . According to previous studies [34,35], the nanohardness,  $E_{\text{OCP}}$  and corrosion current density in PBS of traditional Ti6Al4V alloy were  $6.25 \text{ GPa}$ ,  $-0.52 \text{ V}_{\text{SCE}}$  and  $3.88 \times 10^{-7} \text{ A}\cdot\text{cm}^{-2}$ , respectively. Compared to traditional Ti6Al4V alloy, sample 2-4 has higher OCP, lower corrosion current density, and higher nanohardness, indicating that it has superior mechanical properties and corrosion resistance in PBS at  $37^\circ\text{C}$ , which may become a new generation of biomedical materials in the future. It's found that the sample with best properties was not the sample with the highest mixing entropy, however, it had medium entropy. This result indicated that during designing composition of multi-components alloys, sometimes alloys with medium entropy could have better properties than those with high entropy. Meanwhile, it further confirmed that the co-deposition technique was an efficient approach to develop alloy composition with high performance for biomedical application.

#### 4. Conclusion

In summary, 16 independent samples of Ti-Zr-Nb-Ta biomedical HEA samples were prepared by a new dual-target co-deposition technique with composition gradient distribution, and their microstructure, composition, mechanical properties, and corrosion resistance were systematically studied. Three completely different microstructures were observed in these samples: amorphous, amorphous and  $\text{Ta}_2\text{O}$ , as well as BCC solid solution and  $\text{Ta}_2\text{O}$ . The properties of the samples were jointly affected by composition and phase structure. Considering the mechanical properties and corrosion resistance performance of 16 samples, the sample with chemical composition of  $\text{Ti}_{12.50}\text{Zr}_{11.56}\text{Nb}_{12.71}\text{Ta}_{46.62}\text{O}_{16.61}$  was screened out to have the most outstanding comprehensive performance. Its mixing entropy was  $1.43 \text{ R}$ , and its phase structure was amorphous. The nanohardness, OCP, and corrosion current density of the sample were identified to  $12.91 \pm 0.65 \text{ GPa}$ ,  $-0.37 \text{ V}_{\text{SCE}}$ , and  $3.91 \times 10^{-9} \text{ A}\cdot\text{cm}^{-2}$  respectively, which has superior corrosion resistance and mechanical properties compared to traditional Ti6Al4V alloy. This parallel co-deposition technique and rapid component screening method provides an efficient approach for the development of new advanced biomedical HEAs.

#### CRediT authorship contribution statement

**Xuan Xiao:** Writing – original draft, Investigation, Conceptualization. **Manzhen Lin:** Methodology, Investigation, Formal analysis, Data curation, Conceptualization. **Chenhao Xu:** Methodology, Formal analysis. **Jiawei Zhang:** Methodology. **Wei-Bing Liao:** Writing – review & editing, Supervision, Project administration, Funding acquisition, Formal analysis.

#### Declaration of competing interest

The authors declare that they have no known competing financial interests or personal relationships that could have appeared to influence the work reported in this paper.

#### Data availability

The raw/processed data that support the findings of this study are available on request from the corresponding author.

#### Acknowledgements

This research was supported by the National Natural Science Foundation of China (Grant No. 51801128), Guangdong Basic and Applied Basic Research Foundation (Grant Nos. 2021A1515012278 and 2022A1515010288), and Shenzhen Natural Science Foundation (Grant No. 20231120163549001). Wei-Bing Liao would like to acknowledge the technical support from the Instrumental Analysis Centre of Shenzhen University.

#### References

- [1] Q. Chen, G.A. Thouas, Metallic implant biomaterials, *Materials Science and Engineering R-reports* 87 (2015) 1–57.
- [2] M. Niinomi, Recent research and development in titanium alloys for biomedical applications and healthcare goods, *Sci. Technol. Adv. Mater.* 4 (5) (2003) 445–454.
- [3] J.J. Jacobs, A.K. Skipor, L.M. Patteson, et al., Metal release in patients who have had a primary total hip arthroplasty - a prospective, controlled, longitudinal study, *Journal of Bone and Joint Surgery-American* 80A (10) (1998) 1447–1458.
- [4] M. Zhou, Y. Makino, M. Nose, et al., Phase transition and properties of Ti-Al-N thin films prepared by rf-plasma assisted magnetron sputtering, *Thin Solid Films* 339 (1–2) (1999) 203–208.
- [5] D.R.C. McLachlan, Aluminium and the risk for alzheimer's disease, *Environmetrics* 6 (3) (1995) 233–275.
- [6] B.D. Beake, T.W. Liskiewicz, Comparison of nano-fretting and nano-scratch tests on biomedical materials, *Tribol. Int.* 63 (2013) 123–131.
- [7] S. Bruschi, R. Bertolini, F. Medeossi, et al., Case study: the application of machining-conditioning to improve the wear resistance of Ti6Al4V surfaces for human hip implants, *Wear* 394 (2018) 134–142.
- [8] M.Z. Ibrahim, A.A.D. Sarhan, F. Yusuf, et al., Biomedical materials and techniques to improve the tribological, mechanical and biomedical properties of orthopedic implants - a review article, *J. Alloys Compd.* 714 (2017) 636–667.
- [9] N. Diomidis, S. Mischor, N.S. More, et al., Triboelectrochemical characterization of metallic biomaterials for total joint replacement, *Acta Biomater.* 8 (2) (2012) 852–859.
- [10] J.W. Yeh, S.K. Chen, J.Y. Gan, et al., Formation of simple crystal structures in Cu-Co-Ni-Cr-Al-Fe-Ti-V alloys with multiprincipal metallic elements, *Metallurgical and Materials Transactions a-Physical Metallurgy and Materials Science* 35A (8) (2004) 2533–2536.
- [11] J.W. Yeh, S.Y. Chang, Y.D. Hong, et al., Anomalous decrease in X-ray diffraction intensities of cu-Ni-Al-co-Cr-Fe-Si alloy systems with multi-principal elements, *Mater. Chem. Phys.* 103 (1) (2007) 41–46.
- [12] J.W. Yeh, S.K. Chen, S.J. Lin, et al., Nanostructured high-entropy alloys with multiple principal elements: novel alloy design concepts and outcomes, *Adv. Eng. Mater.* 6 (5) (2004) 299–303.
- [13] D.B. Miracle, O.N. Senkov, A critical review of high entropy alloys and related concepts, *Acta Mater.* 122 (2017) 448–511.
- [14] Z.P. Lu, H. Wang, M.W. Chen, et al., An assessment on the future development of high-entropy alloys: summary from a recent workshop, *Intermetallics* 66 (2015) 67–76.
- [15] Y. Zhang, T.T. Zuo, Z. Tang, et al., Microstructures and properties of high-entropy alloys, *Prog. Mater. Sci.* 61 (2014) 1–93.
- [16] Z.F. Lei, X.J. Liu, Y. Wu, et al., Enhanced strength and ductility in a high-entropy alloy via ordered oxygen complexes, *Nature* 563 (2018) 546–560.
- [17] Y. Zhang, Y.J. Zhou, X.D. Hui, et al., Minor alloying behavior in bulk metallic glasses and high-entropy alloys, *Sci. China Ser. G Phys. Mech. Astron.* 51 (4) (2008) 427–437.
- [18] C.S. Feng, T.W. Lu, T.L. Wang, et al., A novel high-entropy amorphous thin film with high electrical resistivity and outstanding corrosion resistance, *Acta Metallurgica Sinica (English Letters)* 34 (2021) 1537–1545.
- [19] W.B. Liao, C.H. Xu, T.L. Wang, et al., Oxidation influences on the microstructure and mechanical properties of W-Nb-Mo-ta-V-O refractory high-entropy alloy films, *Vacuum* 207 (2023) 111586.
- [20] T.L. Wang, M.A. Khan, C.S. Feng, et al., Parallel preparation of multi-component alloys with composition gradient distribution and their nonlinear microstructures and mechanical properties, *J. Alloys Compd.* 921 (2022) 166159.
- [21] J.J. Hanak, The “multiple-sample concept” in materials research: synthesis, compositional analysis and testing of entire multicomponent systems, *J. Mater. Sci.* 5 (11) (1970) 964–971.
- [22] H. Chang, C. Gao, I. Takeuchi, et al., Combinatorial synthesis and high throughput evaluation of ferroelectric/dielectric thin-film libraries for microwave applications, *Appl. Phys. Lett.* 72 (17) (1998) 2185–2187.
- [23] S.S. Mao, High throughput growth and characterization of thin film materials, *J. Cryst. Growth* 379 (2013) 123–130.

- [24] Y. Sun, Z.C. Lu, X.J. Liu, et al., Prediction of Ti-Zr-Nb-Ta high-entropy alloys with desirable hardness by combining machine learning and experimental data, *Appl. Phys. Lett.* 119 (20) (2021) 201905.
- [25] X.G. Feng, G.Z. Tang, M.R. Sun, et al., Structure and properties of multi-targets magnetron sputtered ZrNbTaTiW multi-elements alloy thin films, *Surf. Coat. Technol.* 228 (2013) S424–S427.
- [26] Y. Zhang, X.H. Yan, J. Ma, et al., Compositional gradient films constructed by sputtering in a multicomponent Ti-Al-(Cr, Fe, Ni) system, *J. Mater. Res.* 33 (19) (2018) 3330–3338.
- [27] M. Niinomi, Recent Titanium R&D for biomedical applications in Japan, *Journal of the Minerals, Metals and Materials Society* 51 (1999) 32–34.
- [28] Q.T. Song, J. Xu, (TiZrNbTa)90Mo10 high-entropy alloy: electrochemical behavior and passive film characterization under exposure to Ringer's solution, *Corros. Sci.* 167 (2020) 108513.
- [29] N. Hua, W.J. Wang, Q.T. Wang, et al., Mechanical, corrosion, and wear properties of biomedical Ti-Zr-Nb-Ta-Mo high entropy alloys, *J. Alloys Compd.* 861 (2020) 157997.
- [30] H. Matsuno, A. Yokoyama, F. Watari, et al., Biocompatibility and osteogenesis of refractory metal implants, titanium, hafnium, niobium, tantalum and rhenium, *Biomaterials* 22 (11) (2001) 1253–1262.
- [31] A. Yamamoto, R. Honma, M. Sumita, Cytotoxicity evaluation of 43 metal salts using murine fibroblasts and osteoblastic cells, *J. Biomed. Mater. Res.* 39 (2) (1998) 331–340.
- [32] H. Cho, K.W. Park, C.H. Park, et al., Abnormally enhanced dielectric constant in ZrO<sub>2</sub>/Ta205 multi-laminate structures by metallic ta formation, *Mater. Lett.* 154 (2015) 148–151.
- [33] Z. Shojaei, G.R. Khayati, E. Darezereshki, Review of electrodeposition methods for the preparation of high-entropy alloys, *Int. J. Miner. Metall. Mater.* 29 (2022) 1683–1696.
- [34] J. Toledano-Serrabona, M.Á. Sánchez-Garcés, C. Gay-Escoda, et al., Mechanical properties and corrosion behavior of Ti6Al4V particles obtained by implantoplasty: an in vitro study. Part II, *Materials* 14 (21) (2021) 6519.
- [35] B. Burnat, M. Walkowiak-przybylo, T. Blaszczyk, et al., Corrosion behaviour of polished and sandblasted titanium alloys in PBS solution, *Acta Bioeng. Biomech.* 15 (1) (2013) 87–95.